

FPGA and computer-vision-based atom tracking technology for scanning probe microscopy

Feng-Du Yu, Li Liu, Su-Ke Wang, Xin-Biao Zhang, Le Lei, Yuan-Zhi Huang, Rui-Song Ma, and Qing Huan

Citation: Chin. Phys. B, 2024, 33 (**5**): 050705. DOI: 10.1088/1674-1056/ad34cb
Journal homepage: http://cpb.iphy.ac.cn; http://iopscience.iop.org/cpb

What follows is a list of articles you may be interested in

FPGA based hardware platform for trapped-ion-based multi-level quantum systems

Ming-Dong Zhu(朱明东), Lin Yan(闫林), Xi Qin(秦熙),Wen-Zhe Zhang(张闻哲), Yiheng Lin(林毅恒), and Jiangfeng Du(杜江峰)
Chin. Phys. B, 2023, 32 (**9**): 090702. DOI: 10.1088/1674-1056/accb48

Real-time programmable coding metasurface antenna for multibeam switching and scanning

Jia-Yu Yu(余佳宇), Qiu-Rong Zheng(郑秋容)†, Bin Zhang(张斌), Jie He(贺杰), Xiang-Ming Hu(胡湘明), and Jie Liu(刘杰)
Chin. Phys. B, 2022, 31 (**9**): 090704. DOI: 10.1088/1674-1056/ac80b2

A high performance fast-Fourier-transform spectrum analyzer for measuring spin noise spectrums

Yu Tong(仝煜), Lin Wang(王淋), Wen-Zhe Zhang(张闻哲), Ming-Dong Zhu(朱明东), Xi Qin(秦熙), Min Jiang(江敏), Xing Rong(荣星), Jiangfeng Du(杜江峰)
Chin. Phys. B, 2020, 29 (**9**): 090704. DOI: 10.1088/1674-1056/ab9c04

Structural and optical characteristic features of RF sputtered CdS/ZnO thin films

Ateyyah M Al-Baradi, Fatimah A Altowairqi, A A Atta, Ali Badawi, Saud A Algarni, Abdulraheem S A Almalki, A M Hassanien, A Alodhayb, A M Kamal, M M El-Nahass
Chin. Phys. B, 2020, 29 (**8**): 080702. DOI: 10.1088/1674-1056/ab90e6

In situ electrical transport measurement of superconductive ultrathin films

Liu Can-Hua (刘灿华), Jia Jin-Feng (贾金锋)
Chin. Phys. B, 2015, 24 (**11**): 110702. DOI: 10.1088/1674-1056/24/11/110702

INSTRUMENTATION AND MEASUREMENT

FPGA and computer-vision-based atom tracking technology for scanning probe microscopy

Feng-Du Yu(俞风度)[1,2], Li Liu(刘利)[1], Su-Ke Wang(王肃珂)[1], Xin-Biao Zhang(张新彪)[3], Le Lei(雷乐)[1], Yuan-Zhi Huang(黄远志)[1,2], Rui-Song Ma(马瑞松)[1], and Qing Huan(郇庆)[1,4,†]

[1] *Beijing National Laboratory for Condensed Matter Physics, Institute of Physics, Chinese Academy of Sciences, Beijing* 100190, *China*
[2] *University of Chinese Academy of Sciences, Beijing* 100049, *China*
[3] *ACME (Beijing) Technology Co., Ltd., Beijing* 101407, *China*
[4] *Key Laboratory for Vacuum Physics, University of Chinese Academy of Sciences, Beijing* 100190, *China*

(Received 27 February 2024; revised manuscript received 13 March 2024; accepted manuscript online 18 March 2024)

Atom tracking technology enhanced with innovative algorithms has been implemented in this study, utilizing a comprehensive suite of controllers and software independently developed domestically. Leveraging an on-board field-programmable gate array (FPGA) with a core frequency of 100 MHz, our system facilitates reading and writing operations across 16 channels, performing discrete incremental proportional-integral-derivative (PID) calculations within 3.4 microseconds. Building upon this foundation, gradient and extremum algorithms are further integrated, incorporating circular and spiral scanning modes with a horizontal movement accuracy of 0.38 pm. This integration enhances the real-time performance and significantly increases the accuracy of atom tracking. Atom tracking achieves an equivalent precision of at least 142 pm on a highly oriented pyrolytic graphite (HOPG) surface under room temperature atmospheric conditions. Through applying computer vision and image processing algorithms, atom tracking can be used when scanning a large area. The techniques primarily consist of two algorithms: the region of interest (ROI)-based feature matching algorithm, which achieves 97.92% accuracy, and the feature description-based matching algorithm, with an impressive 99.99% accuracy. Both implementation approaches have been tested for scanner drift measurements, and these technologies are scalable and applicable in various domains of scanning probe microscopy with broad application prospects in the field of nanoengineering.

Keywords: atom tracking, FPGA, computer vision, drift measurement

PACS: 07.79.Cz, 07.79.–v, 07.05.Pj, 42.30.Tz **DOI:** 10.1088/1674-1056/ad34cb

1. Introduction

Atom tracking technology is a control technique enabling the probe's scanning area to follow regions on the material surface that exhibit specific characteristics, which are predominantly located near local extremal points. This technology is widely used in surface molecular dynamics research,[1–5] scanning drift measurement,[6,7] surface slope measurement, rapid locating and tracking of extreme points,[8] atomic manipulation, etc.

By 1988, the scanning tunneling microscope (STM) was equipped with atom-tracking capabilities using a gradient algorithm and supplementary analog circuits to locate and follow local extrema.[9] With the development of integrated circuit and computer technology, the STM control system has been digitized and continuously upgraded, so it can better complete more and more complex control tasks and process the obtained experimental data in real time, such as atom tracking, fast Fourier transform, spectroscopy tunneling spectroscopy (STS), a variety of image processing methods, etc. These improvements and functions have greatly improved the performance, reliability and experimental flexibility of STM, allowing researchers to delve deeper into the microstructure and properties of material surfaces. Although the atom tracking function is also integrated into some modern STM controllers, the internal implementation methods of these companies are not transparent, and some require additional expenditure. In recent years, some laboratories have also used add-on modules specially designed for fast scanning mode for atom tracking.[10] However, due to the late start of domestic controllers, some functions are not yet complete. Therefore, it is necessary to implement the atom tracking function based on domestic controllers and software.

Atom tracking can be facilitated via hardware or software. The hardware platform has a variety of chips to choose from, and the algorithms implemented are mainly the gradient algorithm, the extremum algorithm and related algorithm variants. In recent years, FPGA chips have seen significant cost reductions and performance enhancements. As a result, these chips are increasingly employed in tasks that demand high precision, real-time processing, and parallel computation capabilities.[11–15] Taking full advantage of FPGA hardware resources and parallel processing capabilities, our method re-

[†]Corresponding author. E-mail: huanq@iphy.ac.cn

© 2024 Chinese Physical Society and IOP Publishing Ltd

duces data processing time, enabling faster real-time atom tracking. With the maturity of machine learning and computer vision technology, it has more and more extensive applications in the field of scanning probe microscope.[16–19] For example, it is able to divide grain boundaries[20] and classify lattice structures,[21] and it can be applied in cell detection and shape distinction.[22] With the help of the software of computer vision, various methods mainly based on feature matching make it possible to achieve atom tracking.[23–25] This paper presents some new approaches to atom tracking, leveraging the superior performance of FPGA and the finesse of modern computer vision techniques. First of all, these two types of implementation methods can realize automatic measurement of drift, and when implemented in hardware, the drift of the scanner shows a certain correlation with its movement mode. The software implementation greatly reduces the workload of manual calibration of atomic displacements and improves the positioning accuracy. At the same time, the performance differences of different algorithms and parameters are also compared. In addition to drift measurement, parameter correction and slope measurement, it also plays an important role in the realms of nanotechnology engineering, advanced materials science and quantum computing, which require precise tracking of atoms.

2. Hardware implementation based on FPGA

2.1. Details of hardware and preliminary preparation

The entire system is a standard STM system with independent intellectual property rights. The current signal is read into the real-time control system by an 18-bit analog-to-digital converter (ADC) after passing through the preamplifier. The real-time control system then controls the movement and bias voltage output of the scanner through a 20-bit digital-to-analog converter (DAC). The real-time control system accepts the control signals and parameters issued by the upstream host software program through the network interface, and returns the data and feedback signals to the upstream host. Figure 1 shows the schematic diagram of the hardware system and the main parts of the hardware control system we have employed. The core of the entire real-time control system is a domestically produced stable and reliable industrial core board, which is mainly composed of TI OMAP-L138 which is a system on chip (SoC), Xilinx xc6slx16 FPGA and Micron D9RZT random access memory (RAM). The SoC has two cores: a digital signal processor (DSP) and a central processing unit (CPU). The SoC and FPGA are connected through buses inside the core board. The network port, external memory interface A(EMIFA), universal serial bus (USB) and other interfaces are led out through the industrial-grade board to board connector to facilitate communication with the host, ADC/DAC, high voltage amplifier (HVA), piezoelectric motor driver (PMD) and other equipment communication. The FPGA internal clock is obtained by multiplying the clock generated by the crystal oscillator through the internal phase locked loop (PLL). FPGA is mainly composed of three major modules: refresh module, PID module and atom tracking module. The refresh module can flexibly configure the reading and writing of 16 channels to increase the effective bandwidth. In order to avoid frequent interactions with the SoC, we also implemented the PID algorithm required for constant current mode on FPGA. First, the logarithmic calculation with a relative error less than 1×10^{-6} across the range of 1–2^{17} is achieved through the implementation of the coordinate rotation digital computer (CORDIC) algorithm and inverse hyperbolic cosine approximation. Subsequently, the discrete-increment PID algorithm which is parameter-adjustable is implemented. Finally, discrete incremental PID operation can be achieved in 3.4 microseconds at the fastest to complete the automatic control of Z-direction motion on the FPGA hardware platform under the condition of 100 MHz main frequency. Based on these foundations, related atom tracking algorithms are implemented to achieve automatic control of the X and Y directions. The control accuracy in the X and Y directions is determined by the relevant algorithms and parameters and the experimental environment. And the FPGA chip is reconfigurable, so the chip can be reprogrammed and loaded with new algorithms without modifying the hardware, giving it good flexibility. FPGA has many kinds of resources, such as lookup table (LUT), lookup table RAM (LUTRAM), block RAM (BRAM), DSP, buffer with universal global (BUFG), and PLL. The resource occupation of each module on the FPGA of the core board is shown in Table 1. Analyzing the consumption ratio of various resources on an FPGA can provide valuable insights for optimizing subsequent designs and selecting FPGA chip types. It is generally advisable to avoid excessively high resource utilization to meet timing requirements for layout and routing and the need for subsequent functional expansions. The table indicates that the DSP resource utilization is as high as 87.5%, while the highest consumption ratio for other resources is only 60.65%. Therefore, for subsequent chip selection, it is advisable to consider FPGA chips with a higher proportion of DSP resources. If there is a desire for more extensive functional expansion, it is necessary to double all resources conservatively estimated.

The ADC module in this system uses the ADI chip to realize AD conversion, producing an 18-bit digital signal with a measurement accuracy of 0.076 mV. The input signal is converted into a differential signal for sampling. The thermostatically controlled chip is used as a voltage reference to improve the sampling accuracy. It is configured with 8 ADC channels via the Altera Cyclone IV FPGA to achieve the conversion of analog signals. The DAC module uses the ADI chip as the DA conversion chip, taking in a 20-bit digital signal and providing an output precision of 0.019 mV. To maintain accuracy,

a chip under constant temperature control serves as the voltage reference, effectively suppressing DAC noise ripple within $V_{pp} \pm 20$ μV. It is configured with 8 DAC channels using the Altera Cyclone IV FPGA to realize the conversion of digital signals. Any surplus input and output channels can be utilized as backups or for potential functional expansion.

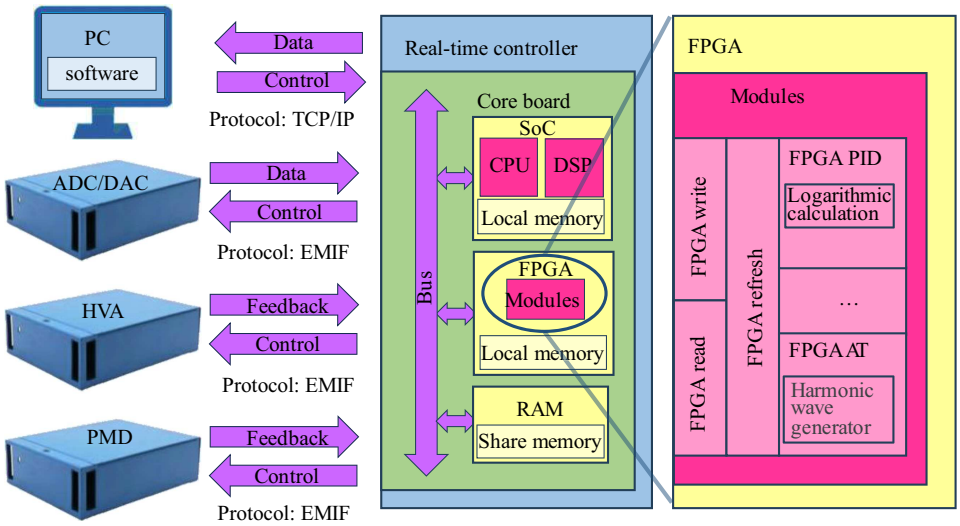


Fig. 1. Block diagram of the core board module of the real-time control system and its interaction with other controlled devices. The main module of FPGA: the refresh module, the PID module, the atom tracking module.

Table 1. FPGA resource occupation of different scopes.

Scope name	Slices	Slice reg	LUT	LUTRAM	BRAM	DSP	BUFG	PLL
Available	2278	18224	9112	2176	32	32	16	2
Totally used	1919	6123	5527	232	2	28	1	1
Refresh module	82	210	156	0	0	0	0	0
PID module	710	1955	1674	142	1	16	0	0
Atom tracking module	814	2493	2291	90	1	12	0	0
Reading module	20	33	16	0	0	0	0	0
Writing module	12	35	14	0	0	0	0	0
Clock module	0	0	0	0	0	0	1	1

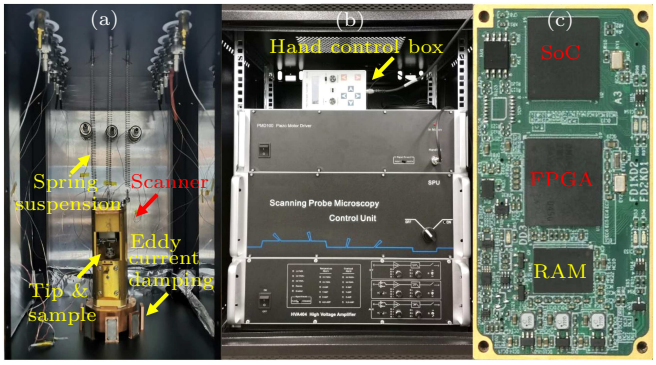


Fig. 2. Experimental system and instruments. (a) Domestic test scanner used in the experiment. (b) Full set of domestic electronic control equipment used in the experiment. (c) Core board of the real-time control system.

The programming language used by the host program is C++, which has excellent performance, flexibility and maintainability. C++ enables the host to efficiently handle various complex tasks, and its cross-platform feature enables the host program to run stably on different operating systems. This program has most of the common functions of general control software, such as coarse motion control, mapping, and STS. The entire domestic STM system can achieve atomic-level resolution imaging. See Fig. 2 for the pictures of each part of the entire system.

2.2. Atom tracking implemented by gradient algorithm

The gradient algorithm is the earliest proposed and commonly used algorithm for atom tracking. The basic principle is to control the probe tip to move consistently with or against the gradient. However, some additional changes are required when implementing the actual digital circuit. Initially, we shall delineate the fundamentals and procedural steps of the gradient algorithm, followed by an examination of its viability across diverse scanning methods.

First of all, in constant current mode, the tip can approximately trace the topography of the material surface. Then the three-dimensional surface can be approximately represented by a binary function $z = f(x,y)$. If the function is continuous and differentiable in the planar region D, for each point, a gradient vector $\frac{\partial f}{\partial x} \cdot \boldsymbol{i} + \frac{\partial f}{\partial y} \cdot \boldsymbol{j}$ can be computed. By moving the probe along or against this vector's direction and repeating this process, it is possible to approach local extreme points within region D. Although this function is non-convex and can only ensure that the final convergent point is a local extremum, this can already meet the needs of some practical applications. When the control is realized through specific digital circuits, discretization and procedural steps are also required to facil-

itate engineering implementation. First of all, since it is implemented through an actual circuit, the partial derivatives in the X and Y directions of a certain central point can only be approximately obtained, and in order to reduce accidental errors, it is best to average multiple times. And stability is crucial for STM, especially since the piezoelectric ceramic actuator also has creep effects and piezoelectric hysteresis, so it is best for the movement trajectory to change continuously and gently without jumps. Therefore, we chose the circular and spiral motion modes with the DAC input waveform shown in Figs. 3(a) and 3(d) to accurately obtain the height change information near the central point. These scanning modes have been proven to have better stability and greater scan rate in STM high-speed imaging.[26–29] The general expression of the relative central point displacement of these two motion modes is as follows:

$$\begin{aligned}\delta x &= u_x \cdot A_{\text{hva}} \cdot k_{\text{piezo}-x} \\ &= A_{u_x} \cdot A_{\text{hva}} \cdot k_{\text{piezo}-x} \cos\omega_x t = A_x \cos\omega_x t, \end{aligned} \tag{1}$$

$$\begin{aligned}\delta y &= u_y \cdot A_{\text{hva}} \cdot k_{\text{piezo}-y} \\ &= A_{u_y} \cdot A_{\text{hva}} \cdot k_{\text{piezo}-y} \sin\omega_y t = A_y \sin\omega_y t. \end{aligned} \tag{2}$$

The alternating current (AC) voltages outputted by the DAC in the x and y directions are u_x and u_y, A_{hva} is the amplification factor of HVA, and $k_{\text{piezo}-x}$ and $k_{\text{piezo}-y}$ are the piezoelectric coefficients in the x and y directions, respectively. A_{u_x} and A_{u_y} are the amplitudes of the output voltage. ω_x and ω_y are the angular frequencies of the output voltage. A_x and A_y are the amplitudes of movement in the x and y directions.

When the displacement is small, the following expression of z can be obtained by approximating the curved surface to a plane. The height change can be expressed as the sum of the change in z value caused by movement in x and y directions respectively: $\delta z = \delta z_x + \delta z_y$. The changes in z value caused by the movement in x direction and y direction can be expressed as

$$\delta z_x = \delta x \cdot \tan\theta_1 = A_x \cos\omega_x t \cdot \tan\theta_1, \tag{3}$$

$$\delta z_y = \delta y \cdot \tan\theta_2 = A_y \sin\omega_y t \cdot \tan\theta_2, \tag{4}$$

where θ_1 is the angle between x-axis and the intersection of x–o–z and the incline, and θ_2 is the angle between y-axis and the intersection of y–o–z and the incline. When the amplitudes in x and y directions are both r, the angular frequencies are the same, and the step length is L, through approximation, then the discrete expressions of the displacements in x and y directions can be directly obtained as

$$\Delta x = \sum_{i=1}^{N} \frac{(z_i - z_0)\cdot L}{r} \cdot \frac{\cos(\varphi_i)}{N} \cdot \frac{2\pi}{C(N)}, \tag{5}$$

$$\Delta y = \sum_{i=1}^{N} \frac{(z_i - z_0)\cdot L}{r} \cdot \frac{\sin(\varphi_i)}{N} \cdot \frac{2\pi}{S(N)}. \tag{6}$$

When N gradually becomes larger, $C(N)$ and $S(N)$ will gradually tend to π which are the integration coefficients determined by discrete points number N. After the above transformation, the formula is converted into an accumulation after calculation of the current value, and the result can be given directly after the last point scan is completed. This allows maintaining the spatial complexity consistently at $O(1)$ without compromising computational speed, with the time complexity consistently held at $O(N)$.

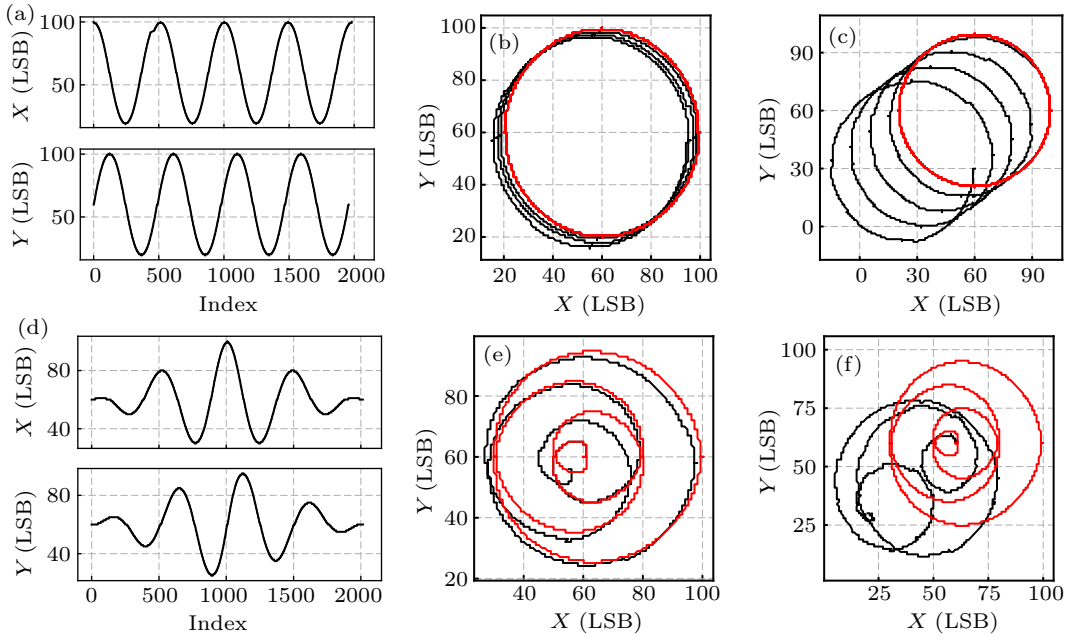


Fig. 3. A comparison of different scanning patterns. (a) and (d) The DAC periodic input waveforms in x direction and y direction in the circular scanning mode and the spiral scanning mode, respectively. (b), (c), (e), (f) The discrete distortions under different scanning modes, black represents the actual relative displacement path, and red represents the displacement path of the tip under ideal conditions: (b), (e) when $R_{\text{scan}}/T_{\text{scan}} \gg$ drift speed ; (c), (f) when $R_{\text{scan}}/T_{\text{scan}} \sim$ drift speed. R_{scan} represents the scanning radius. T_{scan} represents a loop period time. The drift speed is the real drift speed.

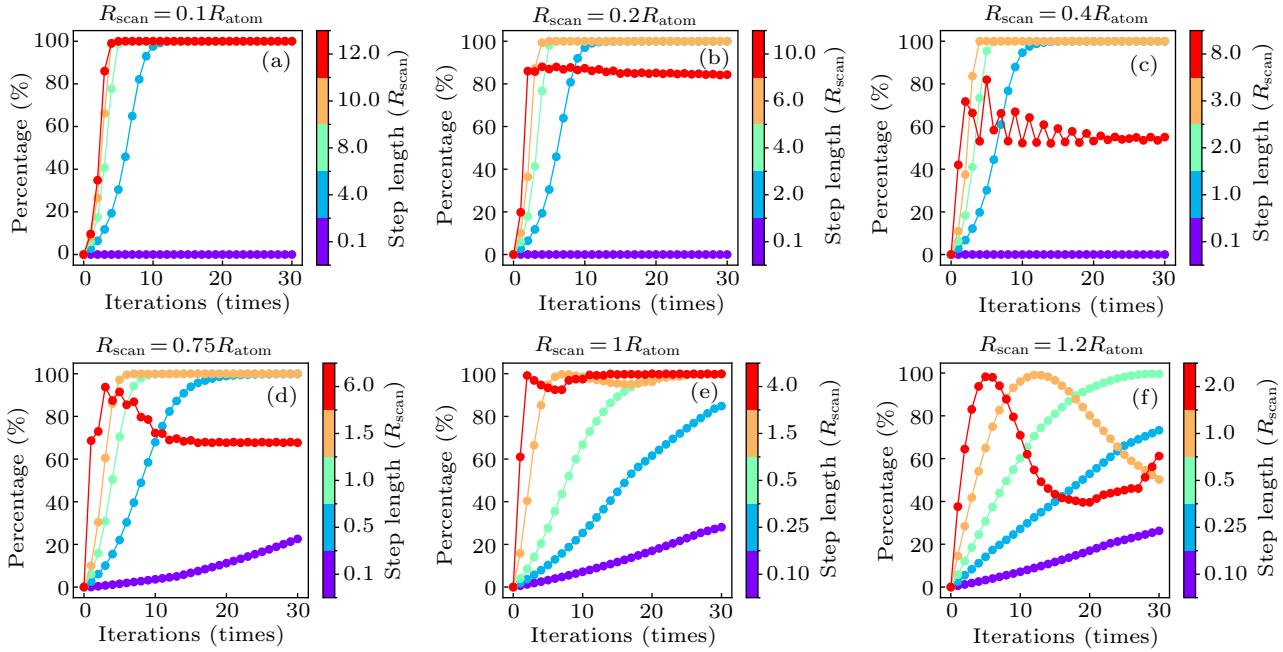


Fig. 4. Parameter simulation image of the gradient algorithm in circular scanning mode. The ratio of the current value to the maximum value changes as the number of iterations increases at different scanning radii.

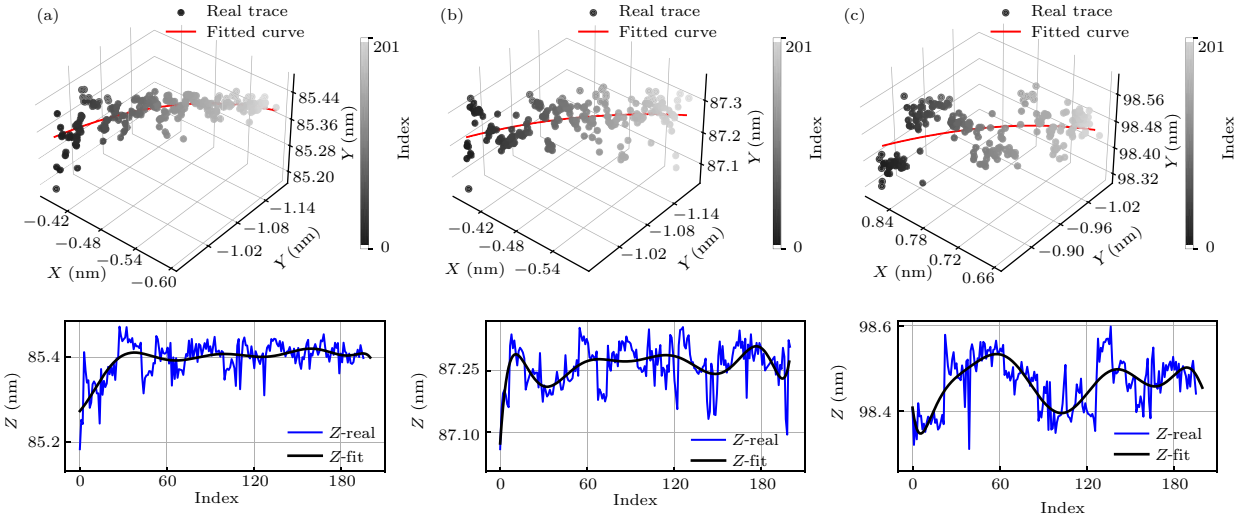


Fig. 5. The tip position and height variations after moving to a lower position by activating atom tracking combining gradient algorithm and circular scanning mode. (a) Scanning radius: 8.36 pm, step length: 4.94 pm. (b) Scanning radius: 8.36 pm, step length: 6.46 pm. (c) Scanning radius: 8.36 pm, step length: 9.84 pm.

Through simulation, the iteration curve obtained by this algorithm with different parameters under ideal conditions is shown in Fig. 4. As the scanning radius increases, when the scanning radius exceeds the atomic radius, fast and stable tracking cannot be achieved no matter how the step size is adjusted, as illustrated in Fig. 4(f). When the scanning radius is small, the step size can be appropriately set larger, but it is best not to exceed the radius of the scanning atoms, otherwise it will easily cause oscillation. As shown in Figs. 4(c) and 4(d), when the step size is set too large, oscillation will occur even if the scanning radius is within a reasonable range. It can be concluded from Fig. 4 that the scanning radius is best not to exceed the atomic radius of the scanned material, and the step size is best not to exceed the scanning radius. The simulation results are closely related to the characteristics and parameters of the three-dimensional model. Very accurate quantitative results of the parameter feasible range cannot be given here, but the above quantitative results give the upper limit of the parameter feasible range in actual situations.

The simulated feasible parameters are used as a reference to assign values to the parameters in the actual implementation of the algorithm. However, we found that the feasible parameter range of the algorithm is far smaller than the ideal parameters of the theoretical simulation when tested at the room temperature. This is mainly because the actual situation is too complex, which includes: (1) the control error in the Z direction, (2) limited effective accuracies of the input and output, (3) approximations in the calculation process of the algorithm,

(4) the influence of drift, (5) the thermal noise of circuits, (6) the creeping effect and electrical hysteresis effect. Under the joint influence of these factors, the actual parameter feasible range becomes smaller, the robustness is poor, and the performance is average at the room temperature with large disturbances. However, under appropriate parameter conditions, a curve that first rises and then fluctuates smoothly can still be obtained. As shown in Fig. 5, we use this algorithm to track the height of atom after moving the tip to a local depression. It can also be clearly seen from the figure that the degree of jitter in Z direction during tracking is greater than that when stable, especially in the initial stage of tracking. When performing atom tracking on the HOPG surface in an atmospheric environment of room temperature, we find that the more appropriate parameter range is $R_{\text{scan}} \sim 0.1R_{\text{atom}}$, step length $\sim 0.5R_{\text{scan}}$. The R_{atom} represents the tracked atom radius. The step length is the coefficient to multiply with gradient.

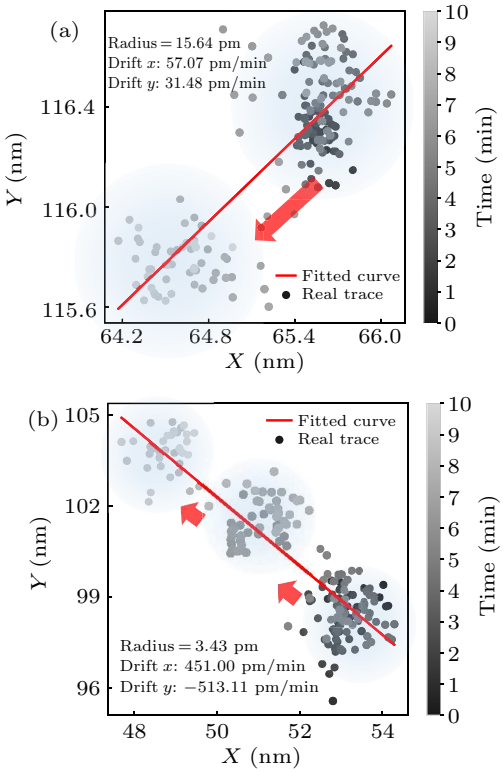


Fig. 6. Overshoot phenomena caused by errors in the gradient algorithm in spiral scanning modes.

Moreover, concerning the gradient algorithm, the spiral scanning pattern is not superior to the circular scanning pattern. From Fig. 3, it is evident that the actual path of the closed spiral scanning pattern is significantly affected by drift, leading to larger errors and, in some cases, an inability to achieve atomic tracking. For instance, in a set of control experiments with a scanning radius fixed at 15.96 pm, the circular scanning pattern only exhibits overshooting and jumping when the step length is set to 4.56 pm. In contrast, the spiral scanning pattern shows overshooting phenomena even at a step length as small as 0.76 pm. Therefore, when using the gradient algorithm, it is best to combine the scanning mode with less impact of distortion such as circular pattern. Of course, no matter what algorithm is chosen, it should be as consistent as possible with $R_{\text{scan}}/T_{\text{scan}} \gg$ drift speed. The overshoot phenomenon is produced when the gradient algorithm is combined with the spiral scanning mode as shown in Fig. 6.

2.3. Atom tracking implemented by extremum algorithm

The principle of the extremum algorithm is to determine the location of the extreme point directly by comparing the value of the Z height. Although it may be affected by some outliers, most of these outliers can be filtered through some filters, making the tracking performance achieved by this algorithm extremely stable. And through the spiral scanning mode, a larger effective scanning range and faster convergence can be achieved.

Figure 7(a) shows a scatter diagram of the tip movement using this algorithm combined with the spiral scanning mode to track surface atoms. The scatter points are fitted using a linear function and represented by a red straight line in the figure. Then use the fitting curve to calculate the drift speed in both X and Y directions. It can be concluded from the figure that as the radius increases, the drift speed also increases. As the radius increases, the degree of dispersion also increases, but the general direction of the drift remains unchanged. As shown in Fig. 7(b), as the radius increases, the coefficient of determination gradually decreases, indicating that the quality of linear drift fitting is gradually getting worse. As shown in Fig. 7(c), as the radius increases, the degree of discreteness of the displacement increases and the stability becomes worse. This shows that the drift of the scanner is related to the scanning mode. Because the drift is driven by temperature, the increase in the scanning radius means that the amplitude of the output voltage becomes larger. The general model of piezoelectric ceramics is a parallel connection of capacitors and resistors, which ultimately leads to an increase in power, thus affecting the drift of the scanner.

While the extremum algorithm combined with the spiral scanning pattern is highly stable due to the algorithm's robustness, it does not imply that the drift of the scanner will also stabilize quickly, which is more influenced by mechanical structures.[30] Short-term measurements are often inaccurate, especially in the early stages of measurement. There may even be drastic changes in the drift direction, as shown in Fig. 8. Therefore, the relative drift direction can only be obtained from long-term measurements and the approximate drift rate can be acquired.

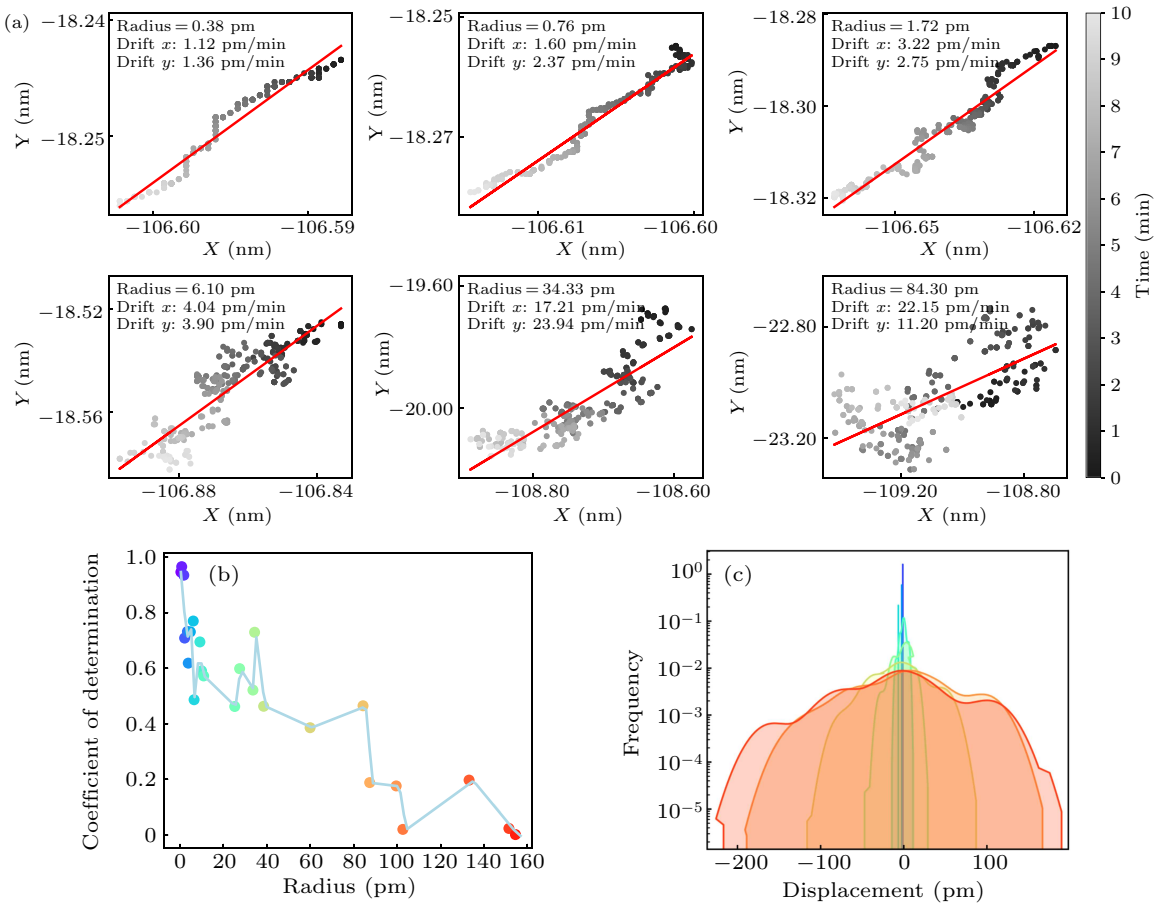


Fig. 7. Extremum algorithm test with spiral scanning pattern. (a) Drift analysis for extremum algorithm with helix scanning pattern under varying radius. (b) Coefficient of determination (R^2) changes with radius. (c) Histogram of displacement distribution with a fitted Gaussian curve.

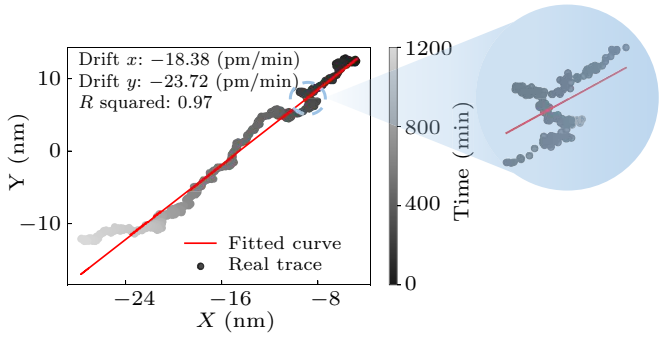


Fig. 8. Long-term drift measured by extremum algorithm with spiral scanning pattern and their recurring phenomena.

3. Software implementation based on computer vision

In addition to achieving atom tracking through hardware implementation, it is possible to employ software programs utilizing computer vision methods for atom tracking. Compared with hardware implementation, software implementation can perform more complex algorithms, has a more powerful processing capability, and can use more image processing and artificial intelligence schemes. And as explained before, drift is correlated with the choice of the scanning pattern used for drift measurement. Therefore, using the drift values obtained through hardware-based approaches which output small alternating voltage may not necessarily be applicable to drift compensation in large-scale scanning. It is recommended to employ the same scanning pattern for drift measurement and utilize the corresponding drift rate for compensation.

However, implementing atom tracking through hardware over a large scanning range poses some challenges. Firstly, the data volume is substantial; for instance, storing a single image with 512×512 pixels requires a minimum of 1 MB of space, and processing a single row requires simultaneous handling of 2 kB of data. Given our current hardware resources, efficiently implementing comprehensive image processing, such as tilt correction or sharpening, is challenging. These processes are crucial for subsequent target recognition. Although complex process and other factors cause software tracking speed to be inevitably slower than that of hardware implementation. However, when scanning the entire picture, a fast tracking speed is not required. Tracking using PC software programs can already meet the requirements. Moreover, using this method for compensation does not require long-term measurements, and can be done as soon as two images are obtained. It is adept at managing frequent fluctuations in both the magnitude and direction of drift.

3.1. Feature matching algorithm based on ROI

The simplest and most intuitive approach is to track the manually determined characteristic area in the scanned image. This characteristic area can be an adsorbed atom or a suspended atom. After tilt correction, the area will be significantly higher than the surrounding areas. The changes of this feature area will be tracked later. This approach represents the first idea of implementing atom tracking based on feature matching in a selected area known as region of interest (ROI).

First, we obtain a starting image and select an appropriate preprocessing method to highlight the characteristic areas in the image as much as possible. Select the most prominent feature area as ROI in the image. Since this area will be the starting area for the next image matching, try to make it contain only the feature area as much as possible. Then you can obtain the next image, first search within a certain range of the previous ROI of the image, and use the template matching method in OpenCV to find the best match. If the matching degree does not reach the set value, further expand the search range until a good enough match is found within the range. Ultimately, before proceeding to the next image, the offset between the ROI's previous position and the optimal matching location is determined, along with the matching score that signifies the match's reliability. The flow chart is shown in Fig. 9(a).

In our application scenario, this method has certain rationality and reliability. Because when the drift during the acquisition of the image is much smaller than the scanning range, the displacement of the feature area between frames is small using pixels as the unit. That is to say, the characteristic area of the next image is likely to be near the characteristic area of the previous image. Therefore, this algorithm is more suitable for this scenario. Figures 10(a), 10(b) and the appendix animation show the atom tracking results of this method.

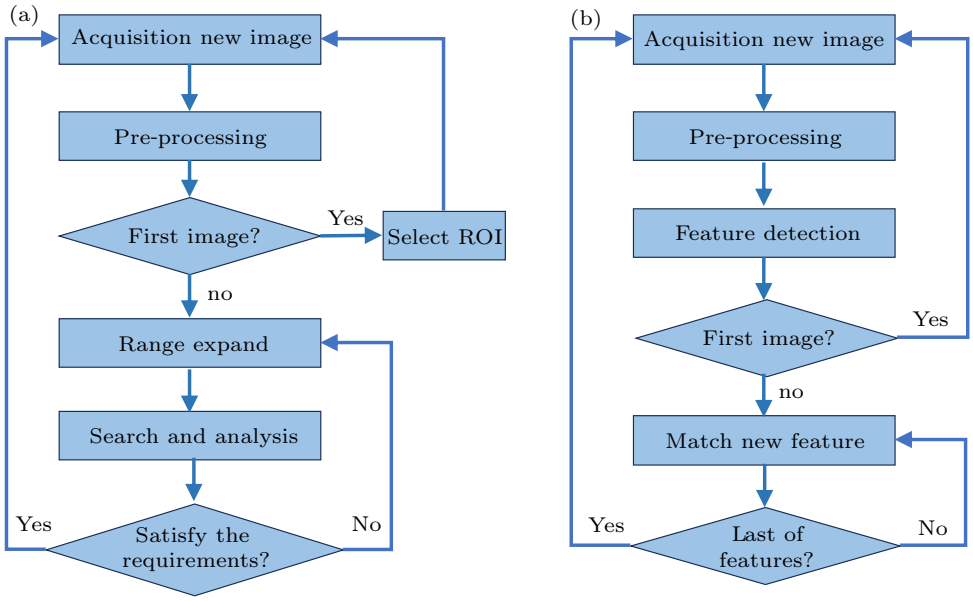


Fig. 9. Image processing flow chart. (a) Feature matching method based on ROI; (b) feature matching method based on feature description.

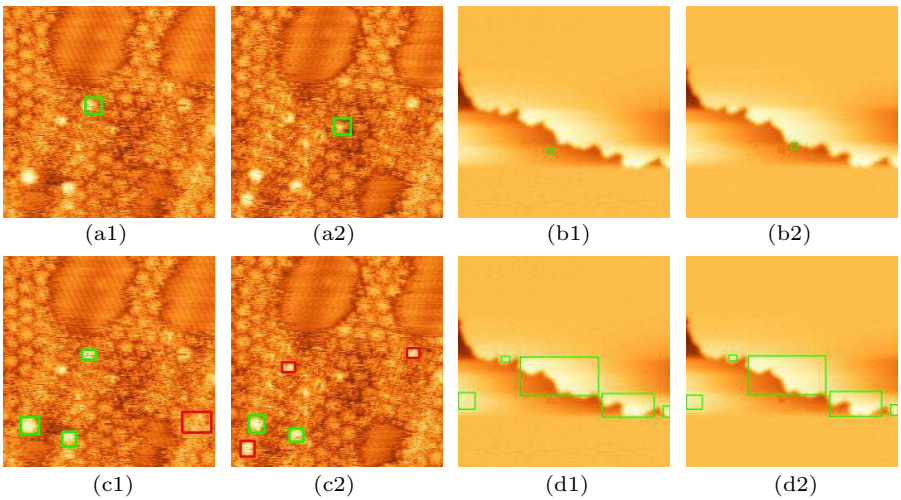


Fig. 10. Comparison of previous and subsequent frames of different image processing methods, where (a), (b) are feature matching methods based on ROI; (c), (d) are feature matching methods based on feature description; 1 and 2 represent the previous and subsequent frames, respectively.

However, some feature areas are unstable and will not always exist. Some will disappear due to physical disturbances, chemical reactions, temperature changes, etc. Due to the disappearance of the selected feature area, tracking for the entire image will be lost. While some characteristic areas disappear, some similar characteristic areas may reappear. We can completely track these feature areas simultaneously. For example, in the two sets of pictures in Figs. 10(a) and 10(b), the human can easily identify the relative displacement of the two images, but the ROI-based algorithm will start tracking other similar feature areas because the originally tracked features disappear. So, a large relative displacement will be obtained.

3.2. Feature matching algorithm based on feature description

The second method is to describe the features that need to be tracked, and let the program automatically find and track feature areas that match the description in the scanned image. As long as the matching areas are recorded, they will be compared with the feature areas of the previous image. The algorithm flow chart is shown in Fig. 9(b). The matching process uses template matching and a strategy of gradually increasing the search range so that the algorithm can handle both small-scale position changes and larger-scale relative displacements, and can flexibly set conditions according to actual needs. If the matching conditions are finally met, it means that the match is successful and is indicated in green. If the match is not successful, the area is indicated by red, as shown in the two sets of pictures in Figs. 10(c) and 10(d). The final relative displacement can be measured by the average relative displacement of all successfully matched feature areas, or by the relative displacement of the area with the highest matching score. This gives the algorithm greater flexibility. And compared with the ROI-based feature matching method, this method can continue to track the remaining feature areas on the entire image even if part of the feature areas disappears, and is more robust. Figure 11 illustrates the scatter diagram depicting the distribution of relative displacement for the two feature matching algorithms. Affected by the disappearance of feature areas, the distribution range of the relative displacement calculated by the feature matching algorithm based on ROI is larger accompanied by obvious jump points. The violin plots for relative displacement in the X and Y directions exhibit noticeable tailing and leaner lines. In contrast, the feature matching algorithm based on feature description yields a smoother transition in relative displacement. The violin plots for relative displacement in the X and Y directions are plumper, without excessively long tails. The results align more closely with the actual changes observed in the dataset we provided.

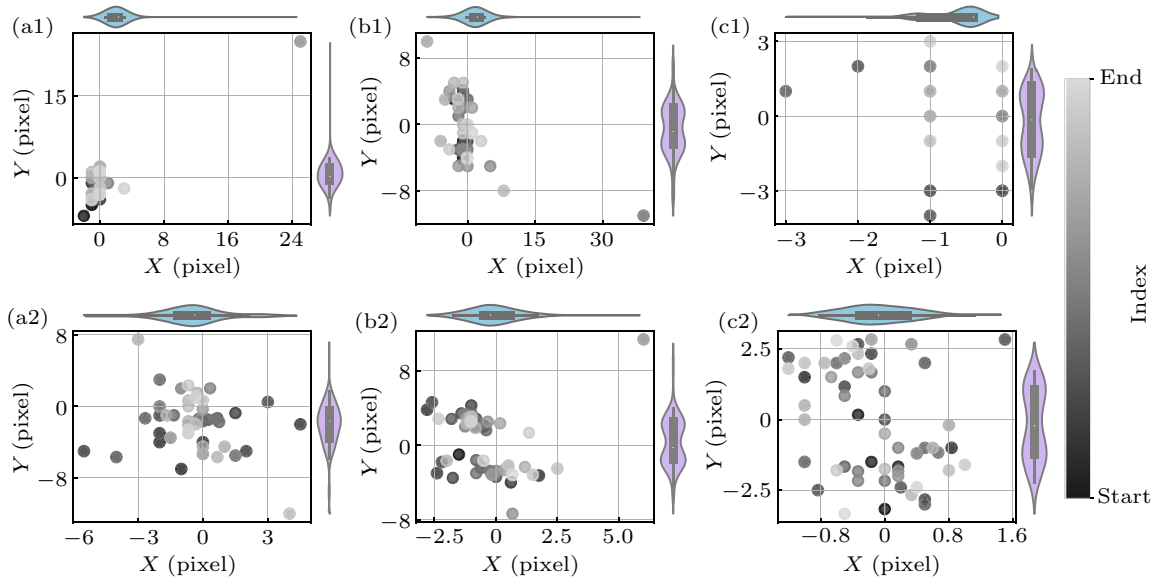


Fig. 11. The relative displacement distribution scatter diagrams of feature areas through computer vision. (a)–(c) represent different data groups respectively. 1 and 2 respectively represent the feature matching algorithm based on ROI and feature description.

The correction implemented through computer vision-based atom tracking requires at least two scanned images before corrections can be applied to the third image. But the advantage is that it can also be tracked and corrected during mapping without the need for additional function switching, thereby enhancing the system stability. Nevertheless, there are obvious shortcomings, such as insufficient tracking speed and low precision.

4. Conclusion and perspectives

We achieved atom tracking through both FPGA and computer vision. Practical measurements of rising curves and long-term drift were conducted. Ultimately, in a room-temperature atmospheric environment on an HOPG surface, stability was reached within dozens of cycles, and the equivalent tracking accuracy was at least 142 pm. The application

of computer vision significantly reduced the manual effort required for parameters calibration and computation, enhancing precision and data processing flexibility. These accomplishments allowed for atom tracking and scanner drift measurement across diverse scenarios. Hardware implementation can also be applied to other SPM systems.[10,31] Furthermore, the software can be implemented in other microscopy fields, such as optical microscopy, electron microscopy,[32–34] and so on.

Data availability statement

The data that support the findings of this study are openly available in GitHub at https://github.com/filliam9560/openSPM.

Acknowledgements

Project supported by the National Science Fund for Distinguished Young Scholars (Grant No. T2125014), the Special Fund for Research on National Major Research Instruments of the National Natural Science Foundation of China (Grant No. 11927808), and the CAS Key Technology Research and Development Team Project (Grant No. GJJSTD20200005).

References

[1] Swartzentruber B S 1996 *Phys. Rev. Lett.* **76** 459
[2] Borovsky B, Krueger M and Ganz E 1999 *Phys. Rev. B* **59** 1598
[3] Hill E, Freelon B and Ganz E 1999 *Phys. Rev. B* **60** 15896
[4] Qin X, Swartzentruber B S and Lagally M 2000 *Phys. Rev. Lett.* **85** 3660
[5] Sato T, Kitamura S I and Iwatsuki M 2000 *Journal of Vacuum Science & Technology A: Vacuum, Surfaces, and Films* **18** 960
[6] Abe M, Sugimoto Y, Custance O and Morita S 2005 *Appl. Phys. Lett.* **87** 173503
[7] Abe M, Sugimoto Y, Namikawa T, Morita K, Oyabu N and Morita S 2007 *Appl. Phys. Lett.* **90** 203103
[8] Guoqiang Y, Anwei L and Xiaotang H 1999 *Aviation Precision Manufacturing Technology* **35** 35
[9] Pohl D W and Möller R 1988 *Rev. Sci. Instrum.* **59** 840
[10] Dri C, Panighel M, Tiemann D, Patera L L, Troiano G, Fukamori Y, Knoller F, Lechner B A J, Cautero G, Giuressi D, Comelli G, Fraxedas J, Africh C and Esch F 2019 *Ultramicroscopy* **205** 49
[11] Jacky J P, Garbini J L, Ettus M and Sidles J A 2008 *Rev. Sci. Instrum.* **79** 123705
[12] Picone R A R, Davis S, Devine C, Garbini J L and Sidles J A 2017 *Rev. Sci. Instrum.* **88** 045108
[13] Ghosal S, Pradhan S and Salapaka M 2018 *Rev. Sci. Instrum.* **89** 056103
[14] Xie S and Ren J 2019 *Mechatronics* **57** 86
[15] Liao H S, Akhtar I, Werner C, Slipets R, Pereda J, Wang J H, Raun E, Norgaard L O, Dons F E and Hwu E E T 2022 *HardwareX* **12** e00341
[16] Kocur V, Hegrova V, Patocka M, Neuman J and Herout A 2023 *Ultramicroscopy* **246** 113666
[17] Rahman Laskar M A and Celano U 2023 *APL Machine Learning* **1** 041501
[18] Stirling J, Woolley R A J and Moriarty P 2013 *Rev. Sci. Instrum.* **84** 113701
[19] Sotres J, Boyd H and Gonzalez-Martinez J F 2021 *Nanoscale* **13** 9193
[20] Liu Y, Yang J, Lawrie B J, Kelley K P, Ziatdinov M, Kalinin S V and Ahmadi M 2023 *ACS Nano* **17** 9647
[21] Choudhary K, Garrity K F, Camp C, Kalinin S V, Vasudevan R, Ziatdinov M and Tavazza F 2021 *Sci. Data* **8** 57
[22] Rade J, Zhang J, Sarkar S, Krishnamurthy A, Ren J and Sarkar A 2022 *Bioengineering (Basel)* **9** 522
[23] Diao Z, Hou L and Abe M 2023 *Appl. Phys. Express* **16** 085002
[24] Diao Z, Ueda K, Hou L, Yamashita H, Custance O and Abe M 2023 *Appl. Phys. Lett.* **122** 121601
[25] Dickbreder T, Sabath F, Holtkemeier L, Bechstein R and Kuhnle A 2023 *Beilstein J. Nanotechnol.* **14** 1225
[26] Teo Y R, Yong Y K and Fleming A J 2016 *American Control Conference (ACC)* Boston Marriott Copley Place, July 6–8, 2016, pp. 7377–7383
[27] Gura L, Yang Z, Brinker M, Kalaß F, Kirstaedter W, Marschalik P, Junkes H, Heyde M and Freund H J 2021 *Appl. Phys. Lett.* **119** 251601
[28] Yang Z, Gura L, Kalass F, Marschalik P, Brinker M, Kirstaedter W, Hartmann J, Thielsch G, Junkes H, Heyde M and Freund H J 2022 *Rev. Sci. Instrum.* **93** 053704
[29] Teo Y R, Yong Y and Fleming A J 2016 *Asian Journal of Control* **20** 1352
[30] Marinello F, Balcon M, Schiavuta P, Carmignato S and Savio E 2011 *Measurement Science and Technology* **22** 094016
[31] Esch F, Dri C, Spessot A, Africh C, Cautero G, Giuressi D, Sergo R, Tommasini R and Comelli G 2011 *Rev. Sci. Instrum.* **82** 053702
[32] Nartova A V, Mashukov M Y, Astakhov R R, Kudinov V Y, Matveev A V and Okunev A G 2022 *Catalysts* **12** 135
[33] Kalinin S V, Mukherjee D, Roccapriore K, Blaiszik B J, Ghosh A, Ziatdinov M A, Al-Najjar A, Doty C, Akers S, Rao N S, Agar J C and Spurgeon S R 2023 *npj Computational Materials* **9** 227
[34] Khan A, Lee C H, Huang P Y and Clark B K 2023 *npj Computational Materials* **9** 85